

Dynamical Electromagnetic fields and Dynamical Electromagnetic Anomaly in heavy ion collisions at intermediate energies

Irfan Siddique,^{1,*} Anping Huang,^{2,†} Mei Huang,^{1,‡} and Muhammad Abdul Wasaye³

¹*School of Nuclear Science and Technology, University of Chinese Academy of Sciences, Beijing 101408, China.*

²*School of Material Science and Physics, China University of Mining and Technology, Xuzhou 221116, China.*

³*School of Computer Science and Engineering, Hunan Institute of Technology, Hengyang 421001, Hunan, China.*

Electromagnetic field produced in non-central heavy ion collisions play a crucial role in phenomena such as chiral anomalous effects, directed flow of mesons and splitting of spin polarization of $\Lambda/\bar{\Lambda}$. A precise description of these fields is essential for quantitatively studying these effects. We investigate the space-time evolution of the electromagnetic fields by numerically solving Maxwell's equations using the results from the UrQMD model, rather than relying on an ansatz. We present the space-averaged dynamic electromagnetic fields, weighted by energy density, in the central region of heavy-ion collisions. These measurements can serve as a barometer for assessing the effects induced by magnetic fields. Comparing the fields at geometric center of the collisions, the space-averaged dynamical fields weighted by the energy density are smaller at the early stage but damp much slower at the later stage. We discuss the impact of these space averaged dynamical magnetic fields on the spin polarization and spin alignment in heavy ion collisions. Additionally, we explore the opportunity to study non-perturbative regime of Quantum Electrodynamics (QED) by presenting the simulation results for space averaged dynamical electric field at intermediate collision energies. Finally, the space-averaged dynamical electromagnetic anomaly $\mathbf{E} \cdot \mathbf{B}$ weighted by energy density is also calculated and compared with experimentally measured slope parameter r .

I. INTRODUCTION

High energy heavy ion collisions provide a unique opportunity to study matter under extreme temperatures and densities, as well as under the influence of exceptionally strong electromagnetic (EM) fields. Simple estimates of the magnetic field strength in non-central heavy ion collisions, where ions move relativistically, show that the magnitude can easily reach the hadronic scale $eB \sim m_\pi^2 \sim 10^{18}$ Gauss at the Relativistic Heavy ion Collider (RHIC) and even stronger magnitudes at Large Hadron Collider (LHC) energies [1–8]. In high-energy heavy-ion collisions, the extreme temperatures and/or densities result in nuclear matter undergoing a deconfinement phase transition, giving rise to a novel state of matter known as quark-gluon plasma (QGP). During the initial stages of these collisions, a strong magnetic field is generated, which can significantly contribute to the initial energy density and plays a crucial role in the plasma's evolution [9]. This scenario provides a unique opportunity to explore the interplay between electromagnetic fields and strongly interacting quark and nuclear matter. The influence of strong magnetic fields on QGP has led to the discovery of several novel phenomena, such as chiral magnetic effects, charge dependent directed flow, directed flow of D^0 mesons, spin polarization of hyperons, splitting of spin polarization of the $\Lambda/\bar{\Lambda}$ etc [10–16]. The electromagnetic field also have interesting effects in pair production [17, 18] and transport properties [19–22].

The effects of magnetic fields and related observables in heavy ion collision depends on the strength and evolution of these fields. Particularly to induce an effect on observables, the magnetic fields needs to be strong enough and sufficiently long lived in the evolving matter in heavy ion collisions. While the initial spatial distribution and strength can be accurately calculated at the beginning of heavy ion collisions, the situation becomes increasingly complex over time as the system evolves through various phase transitions. This complexity makes precise calculations challenging at later stage. Typically, the simulation of electromagnetic fields begins by determining the charge density of the colliding nuclei, which is often achieved using the Woods-Saxon distribution or by sampling charge positions within the nucleus via the Monte Carlo Glauber model [4, 6, 23]. The nucleons are then boosted in opposite direction (usually $\pm z$ directions) and allowed to collide. The simplest approach assumes that the two colliding nuclei pass through each other without further interaction. However, more sophisticated and realistic methods involve using transport models such as UrQMD (Ultra Relativistic Quantum Molecular Dynamics) [24, 25], AMPT (A multiphase transport model) [26, 27] etc. These models help in simulating the entire collisions process and provide a more detailed framework for calculating the evolution of electromagnetic fields.

To calculate the space-time evolution of electromagnetic fields, one generally assumes either the absence of a medium (vacuum scenario) or the presence of the medium such as QGP. Previous studies have shown that in the vacuum scenario, magnetic fields decays rapidly with time, following t^{-3} dependence during the early phases of evolving matter [15, 28]. However, the time evolution of these fields can be significantly modified when consider-

* irfansiddique@ucas.ac.cn

† huanganping@ucas.ac.cn

‡ huangmei@ucas.ac.cn

ing the feedback from QGP medium. Specifically, the decay of the magnetic field is significantly slowed when the feedback from the quark-gluon plasma (QGP) is taken into consideration. [7, 8, 23, 29–33]. To describe the induced effects of electromagnetic fields, it is crucial to understand the quantitative behavior of electromagnetic fields using a more realistic approach. This requires a framework that incorporate the entire collision process and solves the Maxwell's equations in the presence of a conducting medium such as QGP, where induced Faraday currents significantly slows down the decay of produced fields. In this work instead of relying on ansatz, we simulate the full collision process using the UrQMD model to calculate the corresponding currents. We then numerically solve Maxwell's equations, incorporating finite conductivities, to obtain the dynamical electric and magnetic fields. We also provide a comparison with the vacuum scenario. Furthermore, we also extend our calculations to evaluate electromagnetic anomaly $\mathbf{E} \cdot \mathbf{B}$ from the dynamical electric and magnetic fields.

We present numerical results for collision energy in the range of $3.5 \text{ GeV} \leq \sqrt{s_{NN}} \leq 27 \text{ GeV}$ in this work. It is noticed that the dynamics of the system differ significantly between lower and higher collision energies, At lower collision energies, the Landau picture [34, 35] is realised due to the baryon stopping, where after the collision the colliding nuclei are slowed down for a moment and ions may stick together and act as whole gigantic ion which can create strong Columb electric field, which may as well subsequently influence the evolution of electromagnetic fields produced in heavy ion collisions. In contrast, at higher collision energies, Bjorken picture [36] is realised, where due to highly relativistic movement, the colliding nucleons penetrate through each other without significant interaction or sticking together. Moreover, the lifetime of electromagnetic fields is expected to be longer at relatively lower collision energies compared to higher collision energies. The extended lifetime of electromagnetic fields can also play important role in field induced phenomenon.

After providing the brief introduction, in Section II we give the expressions for dynamical electric and magnetic fields in a system having finite conductivities. In Section III, we provide simulation results and discussions for the dynamical electromagnetic fields. Finally we summarize our findings in Section IV.

II. CALCULATION OF DYNAMICAL ELECTROMAGNETIC FIELD

A. Solving Maxwell's Equations: Numerical Methods and Approaches

The covariant form of Maxwell's equation with external sources, given by the current density four-vector

$j^\mu = (\rho, \mathbf{j})$ is:

$$\begin{aligned} \partial_\mu F^{\mu\nu} &= j^\nu, \\ \partial_\mu \tilde{F}^{\mu\nu} &= 0, \end{aligned} \quad (1)$$

where the field strength tensor of electromagnetic field is $F^{\mu\nu} = \partial^\mu A^\nu - \partial^\nu A^\mu$ and it's dual tensor is $\tilde{F}^{\mu\nu} = \frac{1}{2}\epsilon^{\mu\nu\rho\sigma}F_{\rho\sigma}$. The covariant form of Maxwell's equations can be written in a three-vector form as

$$\begin{aligned} \nabla \cdot \mathbf{B} &= 0, \\ \nabla \cdot \mathbf{E} &= \rho, \\ \nabla \times \mathbf{B} &= \partial_t \mathbf{E} + \mathbf{J}_3(\sigma, \sigma_\chi), \\ \nabla \times \mathbf{E} &= -\partial_t \mathbf{B}, \end{aligned} \quad (2)$$

where $\mathbf{J}_3(\sigma, \sigma_\chi) = \mathbf{J}_{ext} + \sigma \mathbf{E} + \sigma_\chi \mathbf{B}$ with \mathbf{J}_{ext} being external current density and ρ being external charge density. In above equation σ is electric conductivity and σ_χ is chiral magnetic conductivity of charged conducting medium (QGP). The first two lines of equation 2 are constraints, while last two lines of equation 2 are used to derive the dynamical electric and magnetic fields.

To evaluate the dynamical electromagnetic fields numerically, we first calculate the j^μ using the UrQMD. The UrQMD model simulate a full collision process, providing the phase-space distribution of all hadrons in a heavy ion collision event. The positions ($x_n(t)$) and momenta ($p_n^\mu(t)$) of charged particle are function of time and are provided by the simulation of UrQMD model. The electric current at a position (t, x) can be given as

$$j^\mu(t, x) = \sum_n \frac{p_n^\mu(t)}{p_n^0(t)} \rho_n(t, x), \quad (3)$$

where n labels n -th hadron. The charged density of n -th hadron (ρ_n) is localized at \mathbf{x}_n , and to account for the finite size of the charge distribution, we smear the charge density by using Gaussian distribution

$$\rho_n(t, x) = \frac{q_n \gamma_n(t)}{(\sqrt{2\pi}\varrho)^3} \exp \left[-\frac{|\mathbf{x} - \mathbf{x}_n(t)|^2}{2\varrho^2} - \frac{\gamma_n^2(t) (\mathbf{v}_n(t) \cdot [\mathbf{x} - \mathbf{x}_n(t)])^2}{2\varrho^2} \right], \quad (4)$$

where q_n is the electric charge, ϱ is the smearing width and γ is the Lorentz factor for the n -th hadron. Once the current density j^μ is calculated with UrQMD we can numerically solve Maxwell equations by constructing corresponding wave equations for the electric and magnetic fields.

In order to numerically solve Maxwell's equations we use strategy as described in [29, 33], we decompose the electric and magnetic field as

$$\mathbf{F} = \mathbf{F}_{ext} + \mathbf{F}_{int}, \quad (5)$$

where \mathbf{F} denotes either \mathbf{B} or \mathbf{E} . In above equation the subscript 'ext' denotes external part of field which is originated by the source contribution from the fast moving

charge particles in heavy ion collisions. The subscripts ‘int’ represents the induced part of field which is generated in the QGP. So Maxwell’s equations given in Eq. (2) can also be separated into external and internal part. The external part is given as

$$\begin{aligned}\nabla \cdot \mathbf{B}_{ext} &= 0, \\ \nabla \cdot \mathbf{E}_{ext} &= \rho, \\ \nabla \times \mathbf{B}_{ext} &= \partial_t \mathbf{E}_{ext} + \mathbf{J}_{ext}, \\ \nabla \times \mathbf{E}_{ext} &= -\partial_t \mathbf{B}_{ext},\end{aligned}\quad (6)$$

whereas the internal part can be given as

$$\begin{aligned}\nabla \cdot \mathbf{B}_{int} &= 0, \\ \nabla \cdot \mathbf{E}_{int} &= 0, \\ \nabla \times \mathbf{B}_{int} &= \partial_t \mathbf{E}_{int} + \sigma (\mathbf{E}_{ext} + \mathbf{E}_{int}) - \sigma_\chi (\mathbf{B}_{ext} + \mathbf{B}_{int}), \\ \nabla \times \mathbf{E}_{int} &= -\partial_t \mathbf{B}_{int}.\end{aligned}\quad (7)$$

We use Yee’s algorithm [37], also known as Finite-Difference Time Domain (FDTD) method to numerically solve above set of equations in space and time, details also in [33]. In FDTD the components of the electric and magnetic field are staggered in both time and space, whereas staggering ensures a second order accuracy on both space and time. For implementation of this algorithm, first we define 3D space with grid steps Δx , Δy , Δz , and define time step such that it satisfies Courant-Friedrichs-Lewy (CFL) stability condition i.e., $\Delta t \leq \left(\sqrt{\frac{1}{\Delta x^2} + \frac{1}{\Delta y^2} + \frac{1}{\Delta z^2}} \right)^{-1}$ and then by using current density j^μ in each grid we initialize the fields. In next step we iterate over time where we update j^μ and so update fields \mathbf{F} (i.e., \mathbf{B} or \mathbf{E}) using finite difference form of $\nabla \times \mathbf{F}$, and also ensure that the fields are updated at each time step. In this way, we can record EM fields at each time step and space grids. The dynamic electric and magnetic fields are obtained by combining results from internal and external components by adding them together as shown in Eq. (5).

B. Space-Average Dynamical Electromagnetic fields weighted Energy Density

The EM fields produced in heavy-ion collisions are highly inhomogeneous in space and time [5, 23, 30, 38, 39], evaluating the field at some specific space-time point could lead to over- or under-estimation of the field induced effects. To mitigate this, we use space-averaged dynamic EM fields weighted by energy density, following the fact that the region with lower energy density contribute less to the chiral effects arising from the electromagnetic field and matter density (details can also be found in [32]). Since we divide the whole space into small grids so space-averaged dynamical fields can be given as

$$\langle \mathbf{F} \rangle_E(t) = \frac{\sum_i \varepsilon_i(t) \mathbf{F}_i(t)}{\sum_i \varepsilon_i(t)}, \quad (8)$$

where $\varepsilon_i(t)$ is the energy density in the i -th grid and \mathbf{F} represents the electric \mathbf{E} or magnetic field \mathbf{B} in the center of the same grid. We use $\langle \dots \rangle_E$ to represent energy density weighted results in our draft. Here we mention that for energy density calculations, we only consider the particles in momentum rapidity range $-0.5 \leq Y \leq 0.5$ in the fireball. While calculating the current densities and solving Maxwell’s equation to obtain dynamical electric and magnetic fields all charged particles from UrQMD are taken into account.

III. SIMULATION RESULTS AND DISCUSSIONS

In this section, we present the simulation results by using the numerical method discussed in the previous section. We assume that one nucleus moves along $+z$ direction and other along $-z$ direction, with their centers located at $x = b/2$ and $x = -b/2$ respectively, where b is impact parameter and the reaction plane is formed by xz -plane. This setup positions the orbital angular momentum (OAM) direction along the $-y$ direction. In set of Maxwell’s equation, we set the electric conductivity $\sigma = 5.8$ MeV, consistent with the lattice quantum chromodynamics calculation [40, 41]. The chiral magnetic conductivity is set to $\sigma_\chi = 1.5$ MeV, corresponding to $\mu_5 \sim 100$ MeV, as used in earlier studies [23, 30, 42]. Although the electric conductivity varies with time, however the influence of the time dependent conductivity on the field lifetime during the hydrodynamic evolution is not very significant [43]. Furthermore, it has been shown in [44] that the behavior of time-dependent and constant electric conductivity is similar at both early and late stages of evolution, and at lower energies this difference becomes minimal. Thus as a first step, treating conductivities as constant is a good approximation in using UrQMD model to obtain four-current and solving Maxwell’s equation at intermediate collision energies.

For numerical simulations, we consider Au+Au collisions with a spatial volume as $-15 \text{ fm} \leq x, y \leq 15 \text{ fm}$ with $dx = dy = 0.5 \text{ fm}$, and $-15 \text{ fm} \leq z \leq 15 \text{ fm}$ with $dz = 0.1 \text{ fm}$. The time step is set to $dt = 0.05 \text{ fm}/c$. Eqs 6, 7 and 8 has been numerically solved by using aforementioned Yee’s algorithm to obtain results in this section. Below, we present simulation results for the spatial distribution and time evolution of the dynamical electromagnetic fields.

1. Spatial Distributions of electromagnetic fields:

In Fig. 1, we shows contour plots of the spatial distributions of the dynamical electric and magnetic field components (in units of m_π^2) for Au+Au collisions at $\sqrt{s_{NN}} = 27 \text{ GeV}$ with $b = 9 \text{ fm}$. These distributions are highly inhomogeneous, consistent with findings from previous studies [5, 23, 30, 38, 39]. The figure has two

panels in Fig. 1: Panel A (left) shows the fields at $t = 0.2$ fm/c, and Panel B (right) shows the fields at $t = 4$ fm/c. These two snapshots illustrate the evolution of the fields over time. In Panel A, the spatial distribution of the electromagnetic field components is symmetric because contributions from \mathbf{F}_{int} (the internal fields) are minimal in \mathbf{F}_{tot} . At the early stage, the dominant contribution comes from the fast-moving source charge particles, represented by \mathbf{F}_{ext} . In Panel B, the spatial distribution becomes partially asymmetric due to the significant contribution from \mathbf{F}_{int} , which includes the effects of electric and chiral magnetic conductivities in the QGP. These results highlight the transition from a purely external field contribution at early times to a combined contribution from both external and internal fields as the system evolves.

We further provide spatial distribution of the product of energy density and magnetic field along the OAM direction (εB_y) in Fig. 2. This calculation is crucial for evaluating energy density-weighted fields, which serve as a barometer for field-induced effects. As described in the previous section, energy density calculations only include particles within the momentum mid-rapidity range $-0.5 < Y < 0.5$ to minimize the influence of spectators and boundary regions of quark or nuclear matter. This ensures that the focus remains on the central region, where εB_y is non-vanishing. The spatial distribution of εB_y clearly indicates that significant contributions are concentrated in the central region of the fireball, reflecting the dominance of QGP effects in this area.

2. Time evolution of the magnetic field:

In this subsection, we discuss the time evolution of the dynamical magnetic fields. In Fig. 3, we give the comparison between vacuum case (B_{y-ext} at (0,0,0), black line), dynamical magnetic field (B_{y-dyn} at (0,0,0), red line) and space averaged dynamical magnetic field weighted by energy density (B_{SA-dyn} , blue line) in a Au+Au collisions at $\sqrt{s_{NN}} = 27$ GeV and $b = 9$ fm. We focus on the time evolution of only y -component of the magnetic field weighted by energy density $B_{SA-dyn} = \langle B_{y-dyn} \rangle_E$ (E labels for energy as weight) because all other components of magnetic field and electric field are almost vanishing because of symmetric collisions and spatial distributions.

The dynamical magnetic field B_{y-dyn} (red line) initially behaves similar to the vacuum scenario B_{y-ext} (black line). However, at later times, the decay of B_{y-dyn} slowdown due to contributions from the QGP medium, where the conductivities σ and σ_χ play a role. This behavior reflects the time required for QGP-induced effects to build up after the collision. The space-averaged magnetic field $\langle B_{y-dyn} \rangle_E$ (blue line) exhibits an interesting trend when compared to the magnetic field at the origin. At initial times, the magnitude of $\langle B_{y-dyn} \rangle_E$ is smaller. However, at intermediate times, it becomes larger than fields at origin (red and black line) due to contributions

from regions with higher energy density in the fireball. At later times $t > 7$ fm/c $\langle B_{y-dyn} \rangle_E$ and B_{y-dyn} at origin have almost similar magnitude, though $\langle B_{y-dyn} \rangle_E$ remains slightly larger.

In Fig. (4a), we give results for time evolution of $\langle B_{y-dyn} \rangle_E$ for different collision energies. The peak value of $\langle B_{y-dyn} \rangle_E$ increases with collision energy, as the production of magnetic fields is directly related to the movement of charged particles. As collision energy increases the system have fast movements of charges and higher energy densities, so the dynamics of the particles such as momentum and currents they generate also intensify, leading to stronger maximum magnetic fields. Conversely, the lifetime of the space-averaged dynamical magnetic field decreases with increasing collision energy. This inverse relationship arises because as collision energies increases the speed of charges also increases, which causes quick decay of the magnetic field.

We also show the magnitudes $\langle B_{y-dyn} \rangle_E$ at early time ($t = 0.1$ fm/c, square symbols) and late time ($t = 8.0$ fm/c, diamond symbols) in Fig. (4b). At early times, the magnitude increases with collision energy, while at late times, the field magnitude decreases as collision energy increases. This highlights that at lower collision energies, the magnetic field persists longer and larger magnitude at late time in the mid-central rapidity fireball system, despite its smaller peak magnitude.

Now we see the impact of the $\langle B_{y-dyn} \rangle_E$ on observable quantities, such as the splitting between the global spin polarization of Λ and $\bar{\Lambda}$ following references [45–47]. The difference between the global polarization of Λ and $\bar{\Lambda}$ is defined as [12]

$$\Delta\mathcal{P} = \mathcal{P}_\Lambda - \mathcal{P}_{\bar{\Lambda}}, \quad (9)$$

the magnetic field induced global polarization of Λ ($\bar{\Lambda}$) can be calculated as

$$\mathcal{P}_\Lambda(\bar{\Lambda}) = \frac{\mu_\Lambda(\bar{\Lambda})B_y}{T}, \quad (10)$$

where $\mu_\Lambda = -0.613\mu_N$ is magnetic moment of Λ hyperon, with μ_N being nuclear magneton and $\mu_{\bar{\Lambda}} = -\mu_\Lambda$. The temperature T marks the point at which the hyperon spin ceases to evolve and we use $T = 155$ MeV. So Eq. (9) can be given as [44]

$$\Delta\mathcal{P} = 0.0826 \frac{B_y}{m_\pi^2}. \quad (11)$$

The numerical results presented in Fig. 4 show that the $\langle B_{y-dyn} \rangle_E$ at initial and intermediate time has magnitude of order $10^{-2} - 10^{-1} m_\pi^2$, and the magnitude at late time is of order $10^{-3} - 10^{-2} m_\pi^2$. The effect of $\langle B_{y-dyn} \rangle_E$ is negligible on the splitting between the global polarization of Λ and $\bar{\Lambda}$. Our result is consistent with the results reported in [44, 47] and with recent STAR data [48].

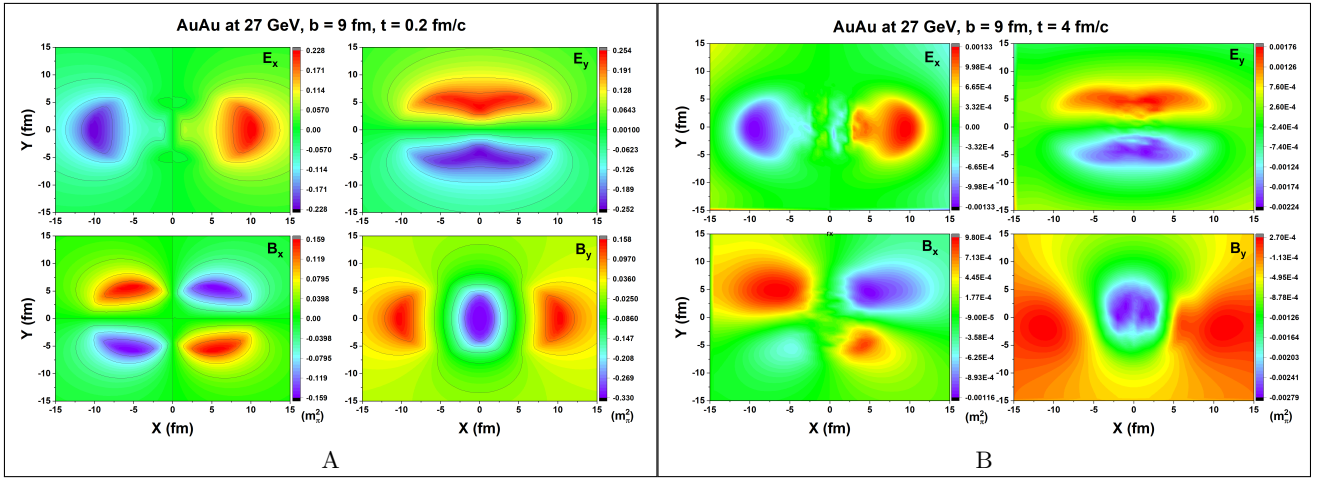


Figure 1. Spatial distribution of transverse components of the dynamical electric and magnetic field in transverse plane in Au+Au collisions at 27 GeV and $b = 9$ fm at $t = 0.2$ fm/c (panel A) and $t = 4$ fm/c (panel B).

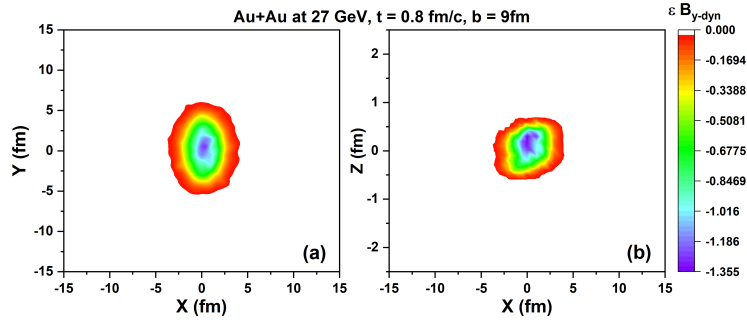


Figure 2. Spatial distribution of the product of energy density and dynamical eB_y in transverse (a) and reaction plane (b) at $t = 0.8$ fm/c in Au+Au collisions at 27 GeV and $b = 9$ fm.

3. Time evolution of the electric field

In this subsection, we give numerical results for the space-averaged dynamic electric field $\langle \mathbf{E}_{dyn} \rangle_E = \left\langle \sqrt{E_{x-dyn}^2 + E_{y-dyn}^2 + E_{z-dyn}^2} \right\rangle_E$ for Au+Au collisions at intermediate collision energies. We show the time evolution results for $\langle \mathbf{E}_{dyn} \rangle_E$ in units of (m_π^2) for collision energies ranging from 11.5 GeV to 3.5 GeV for two impact parameters i.e, $b = 0$ fm (solid lines) and $b = 9$ fm (dashed lines) in Fig. 5. From the figure, we observe that the electric field magnitude is greater for central collisions ($b = 0$ fm) than for non-central collisions ($b = 9$ fm). Similar to the behavior of the magnetic field, the magnitude of the electric field increases with collision energy. However, the decay of the electric field is slower at smaller collision energies, highlighting the enhanced lifetime of the fields at lower energies.

As shown in [49] that the electric fields produced in central collision at intermediate collisions can provide a unique and novel opportunity to study Quantum Electrodynamics (QED) in the non-perturbative regime beyond Schwinger limit i.e., $eE_{cr} := m_e^2 = (0.511 \text{ MeV})^2$,

where m_e being the electron mass [for details see Ref. [49]. Consider the example of the vacuum pair production by strong electric field, which can be classified as perturbative or non-perturbative based on two dimensionless quantities [50–56]

$$\xi(m) = \frac{eE_0 T}{m} \text{ and } \nu = eE_0 T^2 \quad (12)$$

where ξ is Keldysh parameter [57] or also referred to as the non-linearity parameter [58], m is the mass of the particle to be produced, E_0 is the field strength and T is the field lifetime. If $\xi, \nu \gg 1$, the pair production becomes non-perturbative in the sense that the rate of pair production acquires non-analytical dependencies on e and E_0 as $\exp[-(\text{const}) \times (m^2/eE_0)]$. On the other hand, if $\xi, \nu \ll 1$ the pair production becomes perturbative as the rate of pair production has power dependencies in e and E_0 as $\propto (eE_0/m^2)^n$, where $n \in \mathbf{N}$. From Eq. (12), it is evident that E_0 and T , in addition to m , determine whether pair production occurs in a perturbative or non-perturbative regime. While the maximum field strength E_0 increases with collision energy, the lifetime T decreases. To study the non-perturbative regime

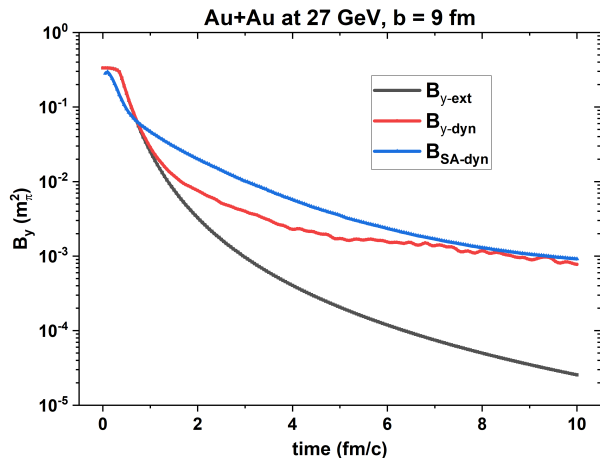


Figure 3. Time evolution of magnetic field B_y in Au+Au collisions at $\sqrt{s_{NN}} = 27$ GeV and $b = 9$ fm. The comparison has been made for B_{y-ext} at $(0,0,0)$, B_{y-dyn} at $(0,0,0)$ and space averaged dynamical magnetic field weighted by energy density ($B_{SA-dyn} = \langle B_{y-dyn} \rangle_E$).

of QED, we need collision energies where E_0 and T are sufficiently large to satisfy $\xi, \nu \gg 1$.

In Fig. (6a), we show the peak magnitude of electric field $_{max} \langle \mathbf{E}_{dyn} \rangle_E$ (MeV scale) as a function of collision energy. The maximum peak strength ranges from 20 MeV to 45 MeV for collision energies between 3.5 GeV to 11.5 GeV. Although the peak field strengths are weaker compared to those at higher collision energies, they are still significantly stronger than the Schwinger limit. The relationship between the peak strength and collision energy is well-fitted by the formula:

$$_{max} \langle \mathbf{E}_{dyn} \rangle_E = 12.997 \times \left(\frac{\sqrt{s_{NN}}}{1 \text{ GeV}} \right)^{1/2}. \quad (13)$$

In Fig. (6b), we give the effective lifetime the electric field, calculated as [49]

$$T = \int_{E(t) > _{max} \langle \mathbf{E}_{dyn} \rangle_E / 2} dt. \quad (14)$$

The results show that T increases as the collision energy decreases and the best fitting curve for T is

$$T = 20.7671 \times \left(\frac{\sqrt{s_{NN}}}{1 \text{ GeV}} \right)^{-1} + 65.8689 \times \left(\frac{\sqrt{s_{NN}}}{1 \text{ GeV}} \right)^{-2}. \quad (15)$$

Our fitting results shown in Eqs. (13) and (15) have different coefficients from the fitting results shown in [49] due to the differences in the transport model and simulation methodology. However, the qualitative behavior remains consistent i.e., at lower collision energies, the electric fields are significantly stronger relative to the Schwinger limit and exhibit much longer lifetimes. This delayed lifetime behavior is attributed to contributions

from internal fields (influenced by conductivities) and baryon stopping at lower collision energies. Similar to [49], our results also indicate that heavy-ion collisions at lower collision energies can provide an excellent opportunity to study the non-perturbative regime of QED. The combination of strong electric fields (beyond the Schwinger limit) and extended lifetimes may allow for the exploration of non-linearity parameters $\xi, \nu \gg 1$ that lead to non-perturbative dependencies. This opens a new avenue for studying fundamental QED processes in extreme conditions.

4. Dynamic electromagnetic anomaly

In this section, we investigate the dynamical electromagnetic anomaly $\mathbf{E} \cdot \mathbf{B}$ in heavy ion collisions. The dynamical electromagnetic anomaly is calculated as

$$\langle \mathbf{E} \cdot \mathbf{B} \rangle_{dyn} = E_{x,tot} B_{x,tot} + E_{y,tot} B_{y,tot} + E_{z,tot} B_{z,tot}, \quad (16)$$

where $F_{i,tot} = F_{i,ext} + F_{i,int}$, with F being E or B . The spatial distribution of $\mathbf{E} \cdot \mathbf{B}$ for Au+Au collisions at $\sqrt{s_{NN}} = 27$ GeV and $b = 9$ fm in transverse plane is given in Fig. 7. Similar to strategy adopted in subsection III 1, there are two snapshots at different time are presented in panel A and panel B belonging to earlier time ($t = 0.8$ fm/c) and later time ($t = 4$ fm/c) respectively of evolving system. In each panel upper plot shows the spatial distribution for $\mathbf{E} \cdot \mathbf{B}$ and lower plot shows the results is for $\varepsilon \langle \mathbf{E} \cdot \mathbf{B} \rangle$, where ε is energy density. From the spatial distribution in the upper plots of both panels A and B of Fig. 7, we observe that the electromagnetic anomaly exhibits a dipolar structure. This dipolar structure is symmetric when flipping the sign of the x -coordinate but asymmetric when flipping the sign of the y -coordinate. In lower plot of each panel of Fig. 7, spatial distribution of $\mathbf{E} \cdot \mathbf{B}$ times energy density (ε) is shown, which also shows a dipolar structure. From the spatial distribution one can notice that directly calculating the dynamical electromagnetic anomaly weighted by energy density will result in $\langle \mathbf{E} \cdot \mathbf{B} \rangle_E \approx 0$, however, when averaging in upper ($y > 0$) and/or lower ($y < 0$) halves of spatial plane, the results are non-zero.

In Fig. (8a), we show time evolution of $\langle \mathbf{E} \cdot \mathbf{B} \rangle_E$ in lower half space i.e., $y < 0$ region in Au+Au collisions at $\sqrt{s_{NN}} = 27$ GeV using formula given in Eq. (8). We give a comparison between $\langle \langle \mathbf{E} \cdot \mathbf{B} \rangle_{ext} \rangle_E$, $\langle \langle \mathbf{E} \cdot \mathbf{B} \rangle_{dyn} \rangle_E$, $\langle \mathbf{E} \cdot \mathbf{B} \rangle_{ext}$ at $(0, -4, 0)$ and $\langle \mathbf{E} \cdot \mathbf{B} \rangle_{dyn}$ at $(0, -4, 0)$ fm. A visible difference can be seen between $\langle \langle \mathbf{E} \cdot \mathbf{B} \rangle_{dyn} \rangle_E$ (solid blue line) and $\langle \langle \mathbf{E} \cdot \mathbf{B} \rangle_{ext} \rangle_E$ (solid green line), we see that initially the magnitude for dynamical fields i.e., $\langle \langle \mathbf{E} \cdot \mathbf{B} \rangle_{dyn} \rangle_E$ and $\langle \mathbf{E} \cdot \mathbf{B} \rangle_{dyn}$ at $(0, -4, 0)$ has smaller magnitude but damps slower than the $\langle \langle \mathbf{E} \cdot \mathbf{B} \rangle_{ext} \rangle_E$ and $\langle \mathbf{E} \cdot \mathbf{B} \rangle_{ext}$ at $(0, -4, 0)$. Notably, the decay of $\langle \langle \mathbf{E} \cdot \mathbf{B} \rangle_{dyn} \rangle_E$ is the slowest among all. The time evol-

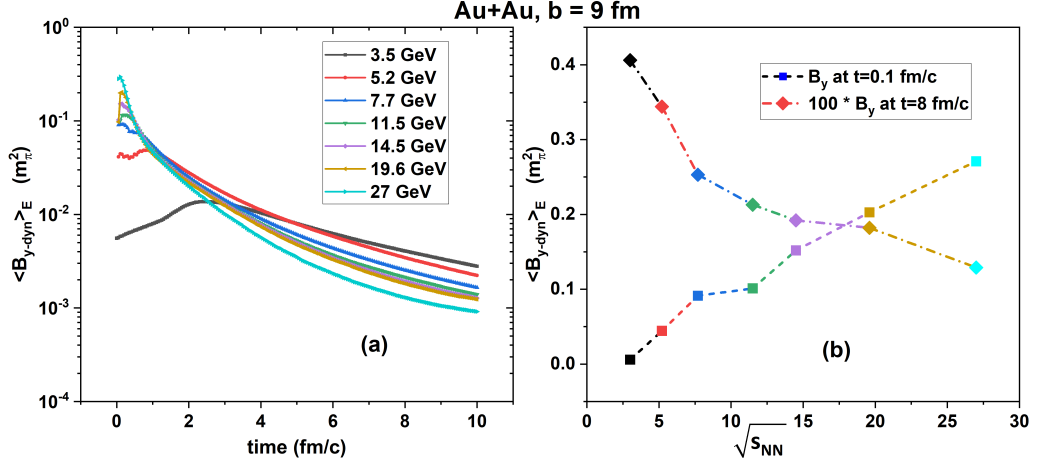


Figure 4. Time evolution of space-averaged dynamical magnetic field $\langle B_{y-dyn} \rangle_E$ as function of collision energy in Au+Au collisions at $b = 9$ fm in left panel. Right panel shows the magnitude of $\langle B_{y-dyn} \rangle_E$ at early time ($t = 0.1$ fm/c) shown by square symbols and later time ($t = 8$ fm/c) shown by diamond symbols.

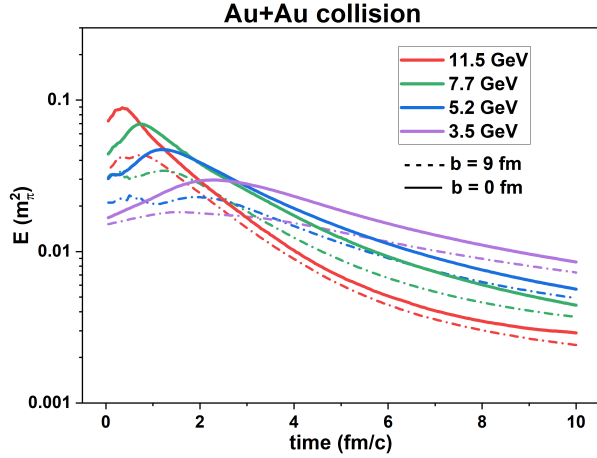


Figure 5. Space-averaged dynamical electric field $\langle E_{dyn} \rangle_E$ as function of collision energy in Au+Au collisions, solid lines are for $b = 0$ fm and dashed lines are for $b = 9$ fm for corresponding collisions energy.

ution of $\langle (\mathbf{E} \cdot \mathbf{B})_{dyn} \rangle_E$ (solid lines) and $(\mathbf{E} \cdot \mathbf{B})_{dyn}$ at $(0, -4, 0)$ for other collision energies is shown in Fig (8b), where we see that, as collision energy decreases, the peak magnitude of $\langle (\mathbf{E} \cdot \mathbf{B})_{dyn} \rangle_E$ decreases, but the decay rate becomes more slower at lower collision energies.

Given the spatial and temporal variation of electromagnetic anomaly in previous figures, their overall effects on physical observable should be evaluated at an average level over the full volume and lifetime of quark and nuclear matter. To quantify net effect by dynamical electromagnetic anomaly we define space-time averaged

dynamical electromagnetic anomaly as

$$\langle (\mathbf{E} \cdot \mathbf{B})_{dyn} \rangle_{TE} = \frac{\int dt \langle (\mathbf{E} \cdot \mathbf{B})_{dyn} \rangle_E}{\int dt}, \quad (17)$$

since we have discretized the whole time period so above equation can be transformed into

$$\langle (\mathbf{E} \cdot \mathbf{B})_{dyn} \rangle_{TE} \equiv \frac{\sum_i \langle (\mathbf{E} \cdot \mathbf{B})_{i,dyn} \rangle_E \Delta t_i}{\sum_i \Delta t_i} \quad (18)$$

where $\langle (\mathbf{E} \cdot \mathbf{B})_{i,dyn} \rangle_E$ is space-averaged dynamical electromagnetic anomaly at i -th time step. As it is shown in Fig (8a) that initially magnitude of $\langle (\mathbf{E} \cdot \mathbf{B})_{dyn} \rangle_E$ decays faster but this decay becomes slower once the contribution from induced part of electric and magnetic field components starts playing role and after $t = 2$ fm/c the decay become rate becomes very slow. Moreover magnitude at $t = 2$ fm/c is much smaller than initial time so we take time average interval $0 \rightarrow 2$ fm/c while calculating $\langle (\mathbf{E} \cdot \mathbf{B})_{dyn} \rangle_{TE}$.

In Fig. 9, we present the space-time averaged magnitude of dynamical electromagnetic anomaly i.e., $\langle (\mathbf{E} \cdot \mathbf{B})_{dyn} \rangle_{TE}$ for different centralities at 27 GeV and compare them to the slope parameter r derived from charge-dependent elliptic flow differences for charged pions, as reported by the STAR collaboration in [59]. The slope parameter r , defined as $v_2(\pi^\pm) = v_2^{\text{base}}(\pi^\pm) \mp r A_{ch}/2$, with $A_{ch} = (N_+ - N_-)/(N_+ + N_-)$ characterizing the charge asymmetry, quantifies the difference in elliptic flow v_2 between π^+ and π^- . The similarity in trends between the space-time averaged dynamical electromagnetic anomaly $\langle (\mathbf{E} \cdot \mathbf{B})_{dyn} \rangle_{TE}$ and the measured r parameter as a function of centrality, as shown in the

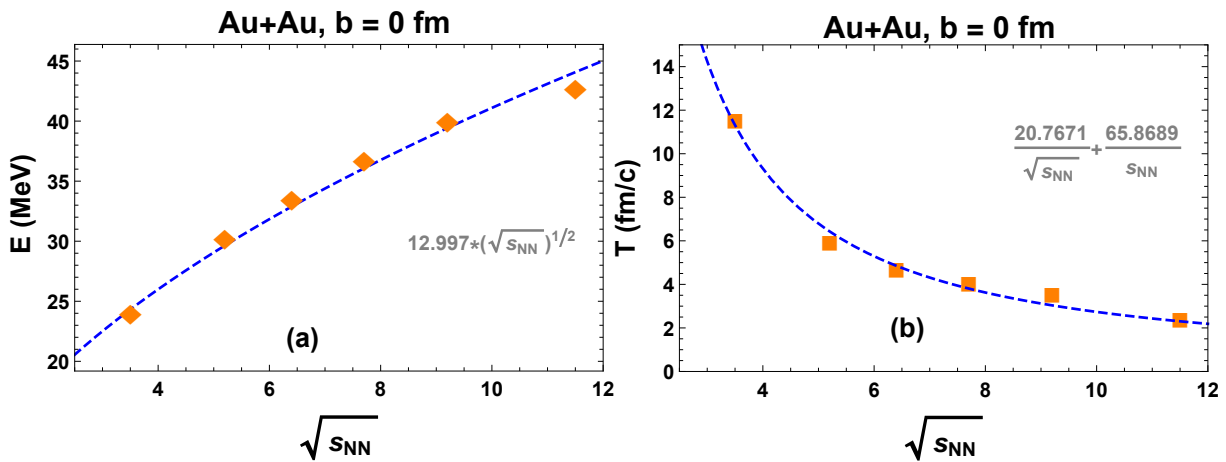


Figure 6. Peak strength of $\langle \mathbf{E}_{dyn} \rangle_E$ as function of collision energy for Au+Au collisions at $b = 0$ fm in left panel. Right panel shows the effective time for $\langle \mathbf{E}_{dyn} \rangle_E$ as a function of collision energy for Au+Au collision at $b = 0$ fm.

Fig. 9, suggests that the QED anomaly $\mathbf{E} \cdot \mathbf{B}$ could also be a potential mechanism for the v_2 separation observed between positive and negative charges in Au+Au collisions at 27 GeV.

IV. SUMMARY AND OUTLOOK

In this study, we have provided a comprehensive analysis of the dynamical electromagnetic fields and dynamical electromagnetic anomaly in heavy-ion collisions, focusing on intermediate collision energies. Using the Ur-QMD transport model, which accounts for full collision process, we calculated the current density and numerically solve Maxwell's equations with finite conductivities to obtain dynamical fields. The research conducted in this papers explores the space-time evolution of dynamical electromagnetic fields and electromagnetic anomaly in the presence of a medium i.e., quark-gluon plasma (QGP). Moreover, space-averaged fields weighted by energy density were introduced to mitigate over- or under-estimations in local field-induced effects.

While studying the dynamical magnetic fields, at intermediate collision energies, we show that they exhibit extended lifetimes and slower decay due to QGP contributions (σ and σ_χ), which may enable a prolonged influence on field-induced phenomena. The peak magnetic field strength increases with collision energy, but at lower collision energies, the fields decay more slowly and persist longer, maintaining a larger magnitude at later times. We also study the impact of the magnetic field on the spin polarization of Λ and $\bar{\Lambda}$. We found that the field strength at later times is insufficient to induce a significant splitting in their global polarization. This result is consistent with previous studies and experimental data from the STAR collaboration.

Dynamical electric fields exhibit behavior similar to magnetic fields, i.e., they exhibit longer lifetimes and

slower decay when medium feedback is considered in terms of conductivities. We also show that the peak electric field strength increases with collision energy, but the lifetime is significantly extended at lower collision energies, which poses the potential of dynamical electric fields in central collisions to probe the non-perturbative regime of QED beyond the Schwinger limit. For collision energies between 3.5 GeV and 11.5 GeV, the maximum electric field strength was found to range from 20 MeV to 45 MeV. While smaller than fields at higher collision energies, these values remain critical for studying the Schwinger effect due to their magnitude and extended lifetime. Our results suggest that intermediate-energy heavy-ion collisions generate non-perturbatively strong electric fields capable of inducing the Schwinger effect. Our results are qualitatively consistent with previous studies. The collisions at intermediate energies may provide a experimental setup to test this phenomenon. However, future work needs to focus and predict the potential experimental signatures of the Schwinger effect in heavy-ion collisions.

Furthermore, we extended our work to study dynamical electromagnetic anomaly. We analyzed the spatial distribution and time evolution of dynamical electromagnetic anomaly. We define and calculate space-time averaged dynamical electromagnetic anomaly and compare them to the slope parameter r . These dependencies are found qualitatively consistent with the STAR data on the slope parameter r as a function of the centrality, indicating the QED anomaly could be a potential mechanism that drives the v_2 separation between positive and negative charges.

In the calculations of this paper, we have used finite conductivities, one can improve by introducing time dependent conductivities, which is expected to further effect the electromagnetic fields and deserves a detailed study in the future. Our study, consistent with previous researches, suggests that intermediate-energy heavy-ion

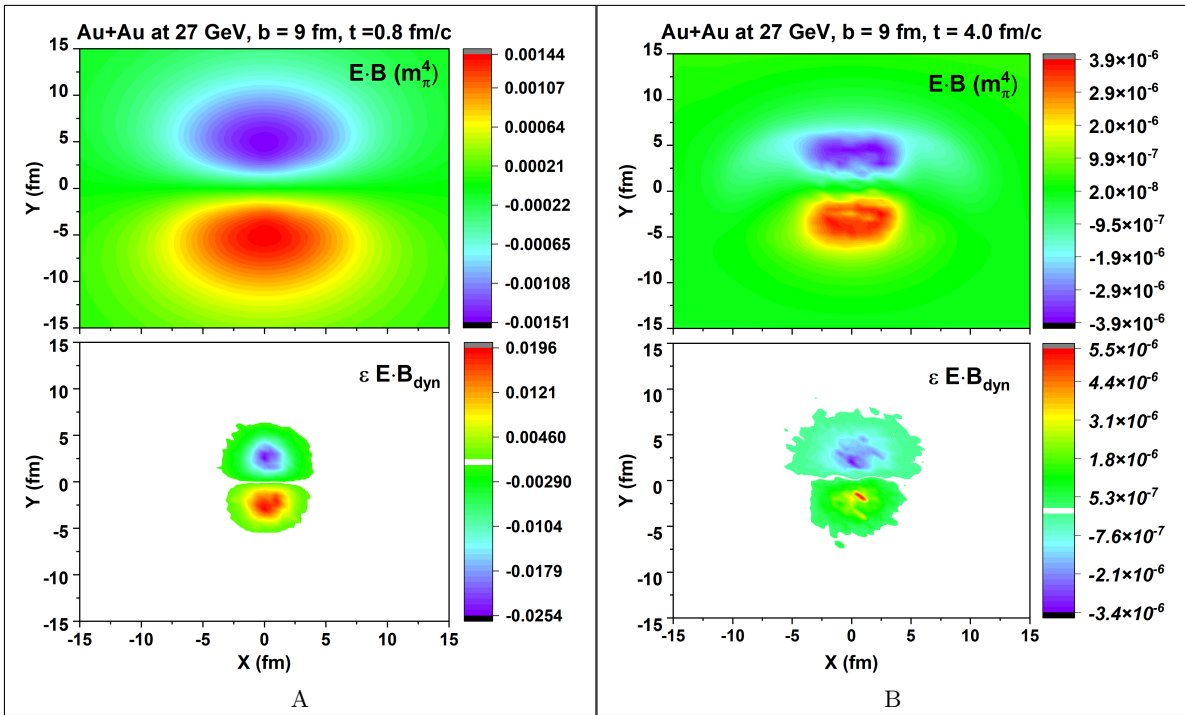


Figure 7. Spatial distribution of dynamical electromagnetic anomaly in transverse plane in Au+Au collisions at 27 GeV and $b = 9$ fm at $t = 0.8$ fm/c (panel A) and $t = 4$ fm/c (panel B). Lower plots of both panel shows spatial distribution for the product of energy density and dynamical electromagnetic anomaly.

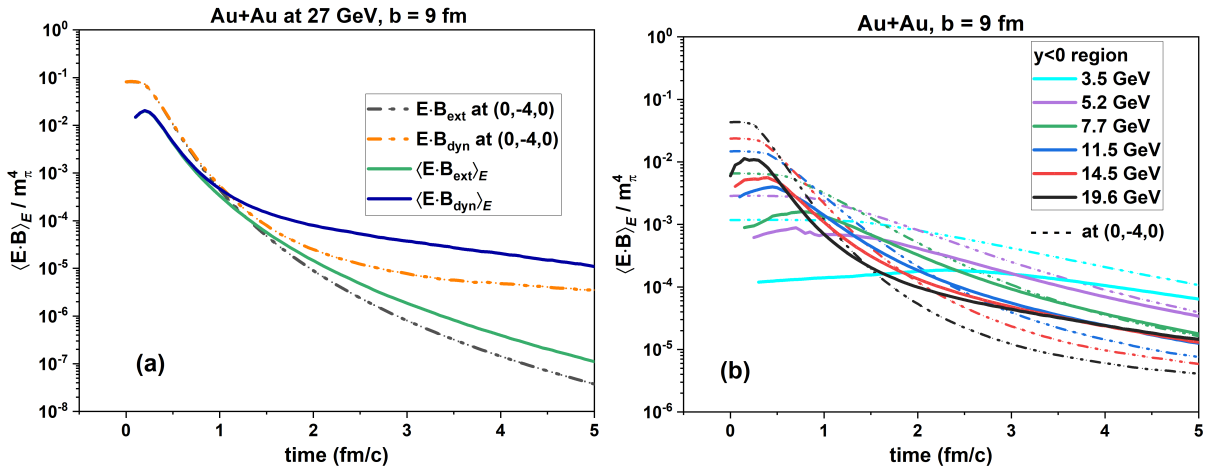


Figure 8. Time evolution of the dynamical electromagnetic anomaly in Au+Au collisions at $\sqrt{s_{NN}} = 27$ GeV and $b = 9$ fm is shown in left panel. Right panel shows the time evolution of electromagnetic anomaly for other intermediate collision energies.

collisions provide a unique opportunity to explore QCD under extreme conditions characterized by strong electric fields. While observing significant effects at the hadronic scale may be challenging, nonperturbative changes are more likely to occur in the deconfined phase of QCD. Numerous studies have investigated QCD in the presence of strong magnetic fields, predicting significant modifications to the QCD phase diagram. However, studies addressing strong electric fields are comparatively sparse and no consensus has been reached regarding their ef-

fects. This highlights the need for further theoretical investigations to understand the impact of strong electric fields on QCD and its phase structure.

ACKNOWLEDGMENTS

We thank X.G. Huang, G.Torrieri and Q. Wang for helpful discussions. I.Siddique is supported by the Ministry of Science and Technology (MOST) of China un-

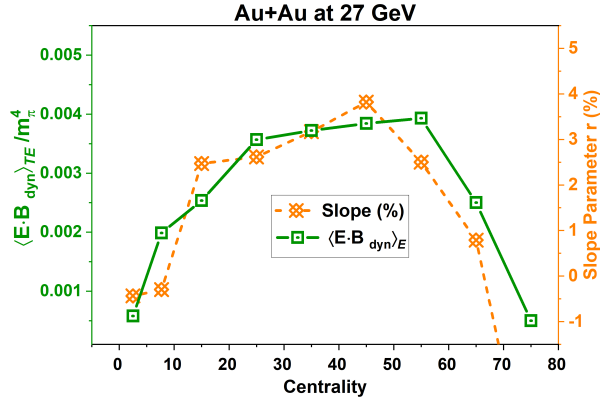


Figure 9. The space-time averaged dynamical electromagnetic anomaly i.e., $\langle \mathbf{E} \cdot \mathbf{B} \rangle_{dyn}$ and the slope parameter r as functions of centrality in Au + Au collisions at 27 GeV.

der Grant No. QN2023205001L and RFIS-NSFC under Grant No. 12350410364. M. Huang and A. Huang are supported by the National Natural Science Foundation of China (NSFC) under Grant No. 12235016 and 12221005. A. Huang is also grateful for the support from the NSFC under Grant No. 12205309.

-
- [1] D. E. Kharzeev, L. D. McLerran, and H. J. Warringa, Nucl. Phys. A **803**, 227 (2008), arXiv:0711.0950.
- [2] V. Skokov, A. Y. Illarionov, and V. Toneev, Int. J. Mod. Phys. A **24**, 5925 (2009), arXiv:0907.1396.
- [3] M. Asakawa, A. Majumder, and B. Muller, Physical Review C **81**, 064912 (2010).
- [4] A. Bzdak and V. Skokov, Phys. Lett. B **710**, 171 (2012), arXiv:1111.1949.
- [5] W.-T. Deng and X.-G. Huang, Phys. Rev. C **85**, 044907 (2012), arXiv:1201.5108.
- [6] J. Błoczyński, X.-G. Huang, X. Zhang, and J. Liao, Phys. Lett. B **718**, 1529 (2013), arXiv:1209.6594.
- [7] K. Tuchin, Phys. Rev. C **88**, 024911 (2013), arXiv:1305.5806.
- [8] K. Tuchin, Phys. Rev. C **91**, 064902 (2015), arXiv:1411.1363.
- [9] V. Roy and S. Pu, Physical Review C **92**, 064902 (2015).
- [10] STAR, M. Abdallah *et al.*, Phys. Rev. C **105**, 014901 (2022), arXiv:2109.00131.
- [11] STAR Collaboration *et al.*, Physics Letters B **839**, 137779 (2022), arXiv:2209.03467.
- [12] STAR Collaboration, Nature **548**, 62 (2017) **548**, 62 (2017), arXiv:1701.06657.
- [13] D. E. Kharzeev, J. Liao, S. A. Voloshin, and G. Wang, Prog. Part. Nucl. Phys. **88**, 1 (2016), arXiv:1511.04050.
- [14] W. Li and G. Wang, Annual Review of Nuclear and Particle Science **70**, 293 (2020).
- [15] X.-G. Huang, Reports on Progress in Physics **79**, 076302 (2016).
- [16] J.-J. Zhang *et al.*, Phys. Rev. Res. **4**, 033138 (2022), arXiv:2201.06171.
- [17] X.-l. Sheng, D. H. Rischke, D. Vasak, and Q. Wang, Eur. Phys. J. A **54**, 21 (2018), arXiv:1707.01388.
- [18] X.-L. Sheng, R.-H. Fang, Q. Wang, and D. H. Rischke, Phys. Rev. D **99**, 056004 (2019), arXiv:1812.01146.
- [19] K. Fukushima, K. Hattori, H.-U. Yee, and Y. Yin, Phys. Rev. D **93**, 074028 (2016), arXiv:1512.03689.
- [20] K. Hattori, X.-G. Huang, D. H. Rischke, and D. Satow, Phys. Rev. D **96**, 094009 (2017), arXiv:1708.00515.
- [21] S. Lin and L. Yang, JHEP **06**, 054 (2021), arXiv:2103.11577.
- [22] H.-H. Peng, X.-L. Sheng, S. Pu, and Q. Wang, Phys. Rev. D **107**, 116006 (2023), arXiv:2304.00519.
- [23] I. Siddique, S. Cao, U. Tabassam, M. Saeed, and M. Waqas, Phys. Rev. C **105**, 054909 (2022), arXiv:2201.09634.
- [24] S. A. Bass *et al.*, Prog. Part. Nucl. Phys. **41**, 225 (1998), nucl-th/9803035.
- [25] M. Bleicher *et al.*, J. Phys. **G25**, 1859 (1999), hep-ph/9909407.
- [26] Z.-W. Lin, C. M. Ko, B.-A. Li, B. Zhang, and S. Pal, Phys. Rev. **C72**, 064901 (2005), arXiv:nucl-th/0411110.
- [27] Z.-W. Lin and L. Zheng, Nuclear Science and Techniques **32** (2021).
- [28] K. Hattori and X.-G. Huang, Nuclear Science and Techniques **28** (2017).
- [29] L. McLerran and V. Skokov, Nucl. Phys. A **929**, 184 (2014), arXiv:1305.0774.
- [30] H. Li, X.-l. Sheng, and Q. Wang, Phys. Rev. C **94**, 044903 (2016), arXiv:1602.02223.
- [31] I. Siddique, R.-j. Wang, S. Pu, and Q. Wang, Phys. Rev. D **99**, 114029 (2019), arXiv:1904.01807.
- [32] I. Siddique, X.-L. Sheng, and Q. Wang, Phys. Rev. C **104**, 034907 (2021), arXiv:2106.00478.
- [33] A. Huang, D. She, S. Shi, M. Huang, and J. Liao, Physical Review C **107**, 034901 (2023).
- [34] E. Fermi, Progress of Theoretical Physics **5**, 570 (1950).
- [35] L. D. Landau, Izv. Akad. Nauk Ser. Fiz. **17**, 51 (1953).
- [36] J. D. Bjorken, Phys. Rev. **D27**, 140 (1983).
- [37] K. Yee, IEEE Transactions on Antennas and Propagation **14**, 302 (1966).
- [38] X.-L. Zhao, G.-L. Ma, and Y.-G. Ma, Phys. Rev. C **99**, 034903 (2019), arXiv:1901.04151.
- [39] X.-L. Zhao, G.-L. Ma, and Y.-G. Ma, Phys. Lett. B **792**, 413 (2019), arXiv:1901.04156.
- [40] H.-T. Ding *et al.*, Physical Review D **83**, 034504 (2011).
- [41] G. Aarts *et al.*, Journal of High Energy Physics **2015** (2015).
- [42] I. Siddique and U. Tabassam, Physical Review C **109**, 034905 (2024).

- [43] K. Tuchin, *Advances in High Energy Physics* **2013**, 1 (2013).
- [44] H. Li, X.-L. Xia, X.-G. Huang, and H. Z. Huang, *Physical Review C* **108**, 044902 (2023).
- [45] F. Becattini, I. Karpenko, M. A. Lisa, I. Upsal, and S. A. Voloshin, *Physical Review C* **95**, 054902 (2017).
- [46] B. Muller and A. Schafer, *Physical Review D* **98**, 071902 (2018).
- [47] H.-H. Peng, S. Wu, R.-j. Wang, D. She, and S. Pu, *Physical Review D* **107**, 096010 (2023).
- [48] M. I. Abdulhamid *et al.*, *Physical Review C* **108**, 014910 (2023).
- [49] H. Taya, T. Nishimura, and A. Ohnishi, *Physical Review C* **110**, 014901 (2024).
- [50] E. Brezin and C. Itzykson, *Physical Review D* **2**, 1191 (1970).
- [51] V. S. Popov, *Zh. Eksp. Teor. Fiz.* **61**, 1334 (1971).
- [52] V. S. Popov, *JETP Lett.* **13**, 185 (1971).
- [53] G. V. Dunne, Q.-h. Wang, H. Gies, and C. Schubert, *Physical Review D* **73**, 065028 (2006).
- [54] T. Oka, *Physical Review B* **86**, 075148 (2012).
- [55] H. Taya, H. Fujii, and K. Itakura, *Physical Review D* **90**, 014039 (2014).
- [56] I. A. Aleksandrov, G. Plunien, and V. M. Shabaev, *Physical Review D* **99**, 016020 (2019).
- [57] L. V. Keldysh, *J. Exp. Theor. Phys.* **20**, 1307 (1965).
- [58] A. Fedotov *et al.*, *Physics Reports* **1010**, 1 (2023).
- [59] STAR, L. Adamczyk *et al.*, *Phys. Rev. Lett.* **114**, 252302 (2015), arXiv:1504.02175.